

Regulator-independent equations of state for neutron stars generated from first principles

J. M. Alarcón,^{1,*} E. Lope-Oter,^{2,†} and J. A. Oller^{3,‡}

¹*Universidad de Alcalá, Grupo de Física Nuclear y de Partículas,
Departamento de Física y Matemáticas, 28805 Alcalá de Henares (Madrid), Spain*

²*Departamento de Física Teórica & IPARCOS,*

Universidad Complutense de Madrid, E-28040 Madrid, Spain

³*Departamento de Física, Universidad de Murcia, E-30071 Murcia, Spain*

We study the equation of state (EoS) of a neutron star (NS) accounting for new advances. In the low energy density, $n \leq 0.1n_s$, with n_s the saturation density, we use a new pure neutron matter EoS that is regulator independent and expressed directly in terms of experimental nucleon-nucleon scattering data. In the highest-density domain our EoS's are matched with pQCD to $\mathcal{O}(\alpha_s^3)$. First principles of causality, thermodynamic consistency and stability are invoked to transit between these two extreme density regimes. The EoS's are further constrained by the new measurements from PREX-II and CREX on the symmetry energy (S_0) and its slope (L). In addition, we also take into consideration the recent experimental measurements of masses and radii of different NSs and tidal deformabilities. A band of allowed EoS's is then obtained. Interestingly, the resulting values within the band for S_0 and L are restricted with remarkably narrower intervals than the input values, with $32.9 \leq S_0 \leq 39.5$ MeV and $37.3 \leq L \leq 69.0$ MeV at the 68% CL. The band of EoS's constructed also allows possible phase transitions (PTs) for NS masses above $2.1 M_\odot$ at 68% CL for $n > 2.5n_s$. We find both long and short coexistence regions during the PT, corresponding to first and second order PTs, respectively. We also generate the band of EoS's when excluding the astrophysical observables. This is of interest to test General Relativity and modified theories of gravity. Our band of EoS's for NSs can be also used to study other NS properties and dark matter capture in NS.

I. INTRODUCTION

Neutron stars (NSs) are among the most dense objects in the universe, and are formed from supernovae explosions of massive stars. The extreme conditions in these compact objects provide a way to study the nuclear matter in a wide range of densities [1]. Neutron stars have been also proposed to study physics beyond the standard model, as dark matter detection, since the intense gravitational field can enhance the capture rate of dark matter particles [2]. In addition, properties of NSs as the tidal deformability, are directly related to the properties of the gravitational-wave signals from a binary NS system [3]. The equation of state (EoS) of a NS is one of the needed inputs for these studies, and its calculation requires techniques employed in nuclear physics and in QCD.

A NS is typically divided into three main regions: the atmosphere, the crust (outer and inner), and the core (outer and inner). The central number density of a NS can reach values that are typically between 5 to 10 times higher than the saturation density. The crust is composed of inhomogeneous nucleonic matter and unlocalized e^- in β -equilibrium [4–6]. The internal constitution of the outermost layers of the crust is well known and the equation of state of this region is determined by experimental atomic mass measurements. The inner crust

of a NS cannot be reproduced in terrestrial laboratories and, therefore, the description of the inner crust must rely on theoretical models. Moving towards the center of the NS, the number density increases, and the nuclei in the crust progressively become more neutron-rich. Eventually, at a certain point known as the neutron-drip point, the number density becomes high enough that neutrons start to leak out from the nuclei, and the inner crust begins. In this regard, at about half the saturation density $n = n_s/2 = 0.08 \text{ fm}^{-3}$, where n is the number baryon density and $n_s = 0.16 \text{ fm}^{-3}$ is the saturation density, corresponding to an energy density $\varepsilon_s \approx 1.8 \times 10^{14} \text{ g/cm}^3 = 70 \text{ MeV fm}^{-3}$, the nuclei completely melts and the NS core would begin. This region is much less understood than the crust and it is divided into outer and inner parts, as in the crust. The core of a NS is supposedly composed of uniform matter at beta-equilibrium, whose properties are strongly related to the symmetry energy originating from the energy difference between pure neutron matter (PNM) and symmetric nuclear matter (SNM).

Direct experimental constraints on NS EoS has improved drastically during recent years thanks to measurements of masses by Saphiro time delay [7–9], NICER telescope of masses and radii from X-ray data [10–14], and gravitational-wave detection from binary NS mergers by the LIGO and Virgo Collaborations [15–17]. Needless to say that all of these data have spurred many theoretical studies to infer valid EoS's [18–35]. In this work, we also attend to this new vigorous impetus on inferring the EoS out of the NS properties. Our novelty here is that we incorporate an EoS for pure PNM at zero temperature

* E-mail: jmanuel.alarcon@uah.es

† E-mail: mariaevl@ucm.es

‡ E-mail: oller@um.es

and very low densities directly expressed in terms of the nucleon scattering data [36], i.e. phase shifts and mixing angles. Let us stress that this EoS is a renormalized result without any regulator dependence, like a cutoff. It stems from the calculation of the neutron-neutron scattering amplitude in PNM as a sum of partial-wave amplitudes, which is then used to resum the ladder series [36–39] for obtaining the energy per neutron E/A . This EoS at low number density is interpolated up to known higher-density results from perturbative QCD (pQCD), applying causality, monotonicity and thermal consistency [40], in two steps. We use a first interpolation between the uncertainty band resulting for the aforementioned EoS [36] for PNM and saturation density, constrained by nuclear experimental data regarding the values of the symmetry energy and its slope [41, 42]. Then, we use a second interpolation between this first band and the high-density pQCD regime [43–45], so we cover a whole range of baryon densities up to around 7 fm^{-3} . All PTs that we find occur for $M \geq 2.1 M_\odot$ at 68 % CL within the range of starting densities between $2.51 n_s \leq n \leq n_c$.

In this last step, we distinguish between two types of procedures, depending on whether we take into account astrophysical observables or not. In one case we use General Relativity (GR) theory to calculate mass and radii of NSs, while in the other only terrestrial experimental results from nuclear physics are accounted for. This is interesting because one can then use the resulting EoS's in the latter case to test modified gravity theories [46, 47].

The contents of the manuscript are organized as follows. In Sec. II we present the method used to compute the EoS at different baryon density regions. In Sec. III we show the results obtained for the different regions, when considering or not astrophysical observables for the computation of the EoS. The results are compared to measurements of masses and radii of different neutron stars, and the tidal deformability-mass relation of GW170817. A summary of the work and conclusions are explained in Sec. IV.

II. METHODOLOGY

The number density inside a neutron star can reach several times the saturation density. Therefore, the calculation of the equation of state combines results in the low and high density regime. In the low density regime, approaches used in nuclear physics as effective field theories (EFTs) or meson exchange models have been typically employed. In the high-density domain, the pQCD results are normally used to constrain the EoS at densities higher than the saturation one. Calculations in pQCD are now available up to $\mathcal{O}(\alpha_s^3)$ [43, 45, 48]. This information can be extrapolated down to lower densities [40] as we apply below. One can also use experimental information at the nuclear saturation density to constrain further the EoS at intermediate densities. In the following, we explain the strategies used in the different density

regions to obtain the EoS of pure neutron matter that will be applied to calculate properties of the neutron stars.

A. Low density region

For the low number density region we use the result for the energy per nucleon (E/A) obtained in [36] by two of the authors. This calculation differs from the standard EFT calculations in several aspects. First, it is a renormalized calculation, and the results for the energy per particle (E/A) are independent of any regulator. However, in present EFT calculations based on Chiral Perturbation Theory there is an explicit and significant (power like) dependence in an unphysical cutoff, such that typically very small variations in this parameter are allowed when discussing results [49, 50]. Second, the results for E/A obtained [36] are expressed in terms of experimental scattering data from nucleon-nucleon interactions in vacuum, namely, phase shifts and mixing angles [51]. However, in EFT calculations a potential has to be first worked out. This implies that its many counterterms needed for a higher-order calculation, like the $N^3\text{LO}$ in Ref. [49, 50], necessarily have to be fitted to a diversity of data, with the caveats that so many free-parameter fits always arise. Third, the chiral EFT calculation in the nuclear medium naively apply the same power counting as in vacuum, while it is well-known [52–54] that the counting gets modified due to the presence of infrared enhanced nucleon propagators when the energy (minus the nucleon mass in a relativistic treatment) through the propagator is $\mathcal{O}(k_F^2/m)$. This implies that the leading order calculation of E/A in the nuclear medium requires to resum the series of ladder diagrams [36, 38, 55]. This is a non-perturbative calculation beyond standard chiral EFT calculations. The formalism for performing this resummation was developed in Ref. [38], and then applied to nuclear matter in Ref. [36]. This theory requires the non-perturbative calculation of the in-medium nucleon-nucleon scattering amplitude by solving the corresponding integral equation [38]. Indeed, as explained in Ref. [36], and also recognized in Ref. [56] within the realm of chiral EFT in-medium calculations, in the dilute limit for nuclear matter non-perturbative effects are important because the nucleon-nucleon system is clearly non-perturbative there due to the presence of the Deuteron in the isoscalar channel and the antibound state in the isovector one, the case of PNM.¹ The integral equation to calculate the nucleon-nucleon partial-wave amplitude in nuclear matter was solved in the limit of contact interactions, and this is why the resulting EoS from Ref. [36] is valid for $k_F \lesssim 150 \text{ MeV}$, or up to a density of $n \lesssim 0.015 \text{ fm}^{-3} \approx 0.1 n_s$. An

¹ This is the reason why higher-order chiral EFT calculations of reference, like those in [49, 50], show E/A for $n > 0.05 \text{ fm}^{-3} \approx 0.3 n_s$.

error estimated for having taking only contact interactions is also evaluated in Ref. [36] by including a Gaussian prefactor in momentum space controlled by a scale Q , with a value around the pion mass. Estimates for higher order beyond the ladder-resummation leading-order result for E/A were also considered, e.g. by appropriately employing a density-dependent neutron mass taken from Ref. [57]. These latter effects were typically much smaller than the uncertainty due to the Gaussian cutoff smearing function (see Ref. [36, 38] for the full formalism and technical details).

The upper value $n \approx 0.015 \text{ fm}^{-3} \approx 0.1 n_s$ for direct applicability of the EoS [36], we call this density limit n_L , is in the density range of the crust of [4, 6]. Thus, no use of any crust EoS is implemented in our interpolations. However, by comparing the calculation in Ref. [6] for the difference in E/A between uniform nucleon matter in β equilibrium and the actual most favorable energetic configuration for the inner crust we observe that this difference at 0.015 fm^{-3} amounts only to around -0.4 MeV , which is well inside the uncertainty band estimated in Ref. [36] at this density. This is clear by comparing Fig. 3 in Ref. [6] with Fig. 5 of Ref. [36]. Additionally, figure 5 of Ref. [6] also predicts a proton fraction of only $\sim 3\%$ at this density.

The resulting E/A from [36] is compared in Fig. 1 with other non-perturbative calculations based on variational techniques [58], on several Quantum Monte Carlo approaches [59–61], on lattice EFT [62], and from N³LO chiral EFT [63]. The EoS of Ref. [36] is given by the black solid line with the gray band reflecting its estimated uncertainty. Except for the lattice EFT calculation [62], we see a remarkable good agreement between these calculations. The only noticeable fact is a trend in [36] to produce slightly larger values of E/A for $n \gtrsim 0.01 \text{ fm}^{-3}$ or $k_F \gtrsim 135 \text{ MeV}$. This is also the case when compared with the perturbative chiral EFT calculations of Refs. [49, 63], cf. Fig. 4 below.

The EoS (pressure P vs energy density ε) of pure neutron matter is extracted from the knowledge of E/A as a function of n , by using the relations

$$\varepsilon = n \left(M_N + \frac{E}{A} \right), \quad (1)$$

and that for $T = 0$,

$$P = n^2 \frac{d(E/A)}{dn} \quad (2)$$

where M_N is the nucleon mass.

Reciprocally, for each point of the EoS with $P(\varepsilon)$ assumed to be known, we obtain the corresponding values of n and E/A by using a discretized version of Eqs. (1) and (2), with the use of dense enough partitions:

$$n_{i+1} = \frac{\varepsilon_{i+1}}{M_N + (E/A)_{i+1}} \quad (3)$$

$$P_i = n_i^2 \frac{(E/A)_{i+1} - (E/A)_{i-1}}{n_{i+1} - n_{i-1}}. \quad (4)$$

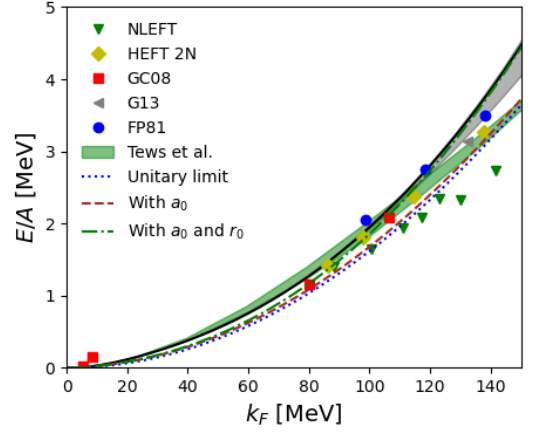


FIG. 1. We show E/A from [36] (black solid line and grey band), and the results for NLEFT [62] (green downwards triangles), HEFT 2N [59] (yellowish green diamonds), the two quantum Monte Carlo calculations of Gezerlis and Carlson [60] (red squares) and Gezerlis *et al.* [61] (gray left-pointing triangles), the variational one of Ref. [58] (blue circles), and N³LO chiral EFT results [63] (green band).

These two equations are employed to solve for $(E/A)_{i+1}$ and n_{i+1} given the earlier two points i and $i-1$, and having at hand $P(\varepsilon)$. Namely, the resulting explicit expressions are:

$$(E/A)_{i+1} = \frac{\Delta_i - 2M_N n_i^2 + \sqrt{\Sigma_i}}{2n_i^2}, \quad (5)$$

$$n_{i+1} = \frac{-\Delta_i + \sqrt{\Sigma_i}}{2P_i},$$

$$\Delta_i = \{(E/A)_{i-1} + M_N\} n_i^2 - n_{i-1} P_i,$$

$$\Sigma_i = \Delta_i^2 + 4n_i^2 P_i \varepsilon_{i+1}.$$

Furthermore, from the grand potential ensemble we calculate the baryon chemical potential μ for each point using the Euler equation

$$\mu_i = \frac{\varepsilon_i + P_i}{n_i}. \quad (6)$$

B. Interpolation process

Starting from the obtained values for $(\varepsilon, P, E/A, n, \mu)$ in the low-density region, we interpolate to higher densities using the interpolation procedure developed in [46]. With this method, the first step is to establish the allowed region based on the conditions of causality and monotonic behavior. In terms of the sound velocity squared c_s^2 ,

$$c_s^2 = \frac{\partial P(\varepsilon)}{\partial \varepsilon}, \quad (7)$$

these conditions imply that $0 \leq c_s^2 \leq 1$. Along the work, we will also indicate when we take another maximum

value for the sound velocity, $c_s^2 \leq 0.781$, according to Refs. [64, 65].

Inside this region, we construct a grid of 1000×1000 candidate points (ε, P) representing potential EoS for the neutron matter. For each grid point ε , we select a value of P of the grid by slowly increasing the slope at the beginning of the grid, and accelerating the slope growth with the energy density with varying values for each EoS, until the maximum slope $c_s^2 \leq 1$ is obtained, thus ensuring the principles of stability and causality. We also account for possible phase transitions (PTs) by increasing ε while $P(\varepsilon)$ is held fixed. Moreover, we also calculate for each point of the EoS the value of μ by means Eqs. (3)–(6), ensuring the thermodynamic consistency principle and the causality of speed of sound in the (n, μ) plane. There, the stability and causality conditions read

$$c_s^{-2} = \frac{\mu}{n} \frac{\partial n(\mu)}{\partial \mu} \geq 1. \quad (8)$$

In addition, in each interpolation, we display the bands related to the integral constraints [40], corresponding to the maximum and minimum $P(\varepsilon)$ values of the high matching band with pQCD. These bands are built according the procedure of Ref. [40]. See this reference for the derivation and explicit expressions of the limiting curves $\{\varepsilon_{\max}(\mu), P_{\min}(\mu, n_{\max}(\mu))\}$ and $\{\varepsilon_{\min}(\mu), P_{\max}(\mu, n_{\min}(\mu))\}$, with $M_N \leq \mu < \mu_H$, and μ_H the upper limit for the chemical potential in the interpolation process.

Following these constructions, we proceed with two interpolations: *i*) From the upper limit of applicability of the EoS [36] in density, n_L , up to the saturation density n_s . *ii*) From n_s up to the pQCD limit of around $40n_s$, with a highest chemical potential $\mu_H = 2600 \pm 8$ MeV. In this way, for the first extrapolation we are able to restrict the information at n_s from experimental information on nuclear reactions, and for the second one the constraints come by requiring the reproduction of the pQCD limiting values. In addition, we have also at our disposal the use of experimental data from astrophysics on neutron stars.

C. First interpolation, $n_s \geq n \geq n_L$

For the first interpolation, the experimental information that we take in order to constrain the EoS at n_s stems from neutron skin measurements in ^{208}Pb by PREX-II [41] and ^{48}Ca by CREX [42] experiments, leading to values for the symmetry energy, S_0 , and its slope, L , at the saturation density $n = n_s$. Here, the symmetry energy as a function of density is defined as $E_{\text{sym}}(n) = (E/A)_{\text{PNM}}(n) - (E/A)_{\text{SNM}}(n)$, and its slope $L_{\text{sym}}(n) = 3n\partial E_{\text{sym}}(n)/\partial n$. In the following, we denote by $S_0 = E_{\text{sym}}(n_s)$ and $L = L_{\text{sym}}(n_s)$.

From PREX-II [41] Ref. [66] deduces the values:

$$S_0 = 38.1 \pm 4.7 \text{ MeV} \quad (9)$$

$$L = 106 \pm 37 \text{ MeV}. \quad (10)$$

In turn, Ref. [67] from the CREX experiment [42] distinguishes between two scenarios and gives two possible values for L_{sym} :

$$\text{Scenario 1: } L = 110 \pm 40 \text{ MeV}, \quad (11)$$

$$\text{Scenario 2: } L = 19 \pm 19 \text{ MeV},$$

and not providing any independent value for S_0 .

Now, our point is to use this information to constraint the energy per particle and pressure for PNM at n_s , by also taking into account that at the equilibrium $P_{\text{SNM}}(n_s) = 0$, and the phenomenological values $(E/A)_{\text{SNM}}(n_s) = -16.0 \pm 0.5$ MeV and $n_s = 0.16 \pm 0.01 \text{ fm}^{-3}$ [68]. Therefore, $(E/A)_{\text{PNM}}(n_s)$ and $P_{\text{PNM}}(n_s)$ can be restricted within experimentally established intervals,

$$(E/A)_{\text{PNM}}(n_s) = E_{\text{sym}}(n_s) + (E/A)_{\text{SNM}}(n_s) \quad (12)$$

$$\in (16.9, 27.3) \text{ MeV},$$

$$P_{\text{PNM}}(n_s) = \frac{1}{3} n_s L_{\text{sym}}(n_s).$$

For the maximum value $L_{\text{sym}}(n_s) = 143$ MeV, we obtain a pressure at saturation density $P_{\text{PNM}}(n_s) = 7.62$ MeV/fm³. By the Euler relation Eq. (6) these values give us the largest limit for a $\mu_H = 1014.5$ MeV used in the construction of the allowed regions within the (ε, p) plane following Ref. [40].

Selecting a minimum value of $P_{\text{PNM}}(n_s)$ from CREX measurements is a much more complicated task, as clearly reflected in Eq. (11). Different Bayesian analyses [18, 67, 69] found that the two experimental results are incompatible with each other at 68% confidence level, but compatible at 95% confidence level. We first select the lowest central value of [67] $L_{\text{sym}} = 19$ MeV, that implies $P_{\text{PNM}}(n_s) \approx 1.01$ MeV/fm³.

Because of this limitation to clearly settle the low limit for L from CREX, we have moved on to the Unitary Gas Conjecture (UGC) to constraint E/A from below [70, 71]. In this model, the energy per particle of a unitary Fermi gas of neutrons $(E/A)_{\text{UG}}$ is taken as a lower bound [70, 71] for E/A in PNM, and it is supported by many explicit calculations. In a unitary Fermi gas the S -wave scattering length is infinity and no other parameters in the effective range expansion nor higher partial waves are included in the neutron-neutron interactions. The resulting expression for $(E/A)_{\text{UG}}$ is universal and given by $(E/A)_{\text{UG}} = \xi(E/A)_F$, where ξ is the Bertsch parameter, $\xi = 0.370(5)(8)$ [72], and $(E/A)_F$ is E/A for a free Fermi gas. By applying Eq. (2) we then have the values $(E/A)_{\text{UG}}(n_s) = 12.7 \pm 0.3$ MeV, $\varepsilon_{\text{UG}}(n_s) = 152.46 \pm 0.05$ MeV/fm³, $P_{\text{UG}}(n_s) = 1.33 \pm 0.04$ MeV/fm³ and $L_{\text{UG}} = 24.9 \pm 0.7$ MeV. By applying Eq. (6) these values imply a chemical potential at n_s equal to $\mu_H = 960.6 \pm 0.6$ MeV. This chemical potential is the smallest limit for a μ_H to be used in the construction of allowed regions of EoS in the (ε, p) plane from Ref. [40].

D. Second interpolation for higher densities, $n > n_s$

For the second extrapolation up to very high densities, the EoS can also be computed directly from the fundamental theory of Quantum Chromodynamics (QCD). This theory becomes perturbative at asymptotically high energies, which are reached either at high temperatures or at high densities, at about 20–40 n_s in baryon number density, well above the densities reached in NS [43, 45, 73, 74]. However, the existence of this pQCD regime implies a limit to the pressure, energy density, and baryon chemical potential at the pQCD matching point. This fact is certainly very interesting because it provides constraints on the EoS and creates a bounded region through which valid EoS $P(\varepsilon)$ must pass. The partial N³LO pQCD results of [45] shows that this regime is valid at $\mu_{pQCD} = 2.6$ GeV and these results still depend on a renormalization scale X [40, 44].² All the points of the EoS can be connected to the pQCD values, $(\mu_{pQCD}, \varepsilon_{pQCD}, P_{pQCD})$, at any point inside the band corresponding to $\mu_{pQCD} = 2.6$ GeV and the renormalization scale $X \in [1, 4]$ [40, 45]. This connection has to be made by some causal, stable and thermodynamically consistent interpolation, taking into account the squared speed of sound in the plane (P, ε) , $c_s^2 = \partial P / \partial \varepsilon \leq 1$, as well as in the plane (n, μ) , $c_s^2 = (n/\mu)(\partial \mu / \partial n \leq 1)$, cf. Eqs. (7) and (8), respectively.

There are different ways to take into account the results of pQCD at high chemical potential, $\mu_H \approx 2.6$ GeV. Some models [75] terminate the extension of the EoS at a certain $n_{\text{term}} = n_c$ (where n_c is the central density number of the NS with the maximum mass possible for a given EoS, when the TOV equations are solved for a non-rotating NS), but others models extrapolate their EoS up to a much higher density $n_{\text{term}} \approx 10n_s$ [32, 76]. The latter references apply the limits for $P(n)$ at every n derived from the integral constraints [40]:

$$\int_{\mu(n)}^{\mu_H} n(\mu) d\mu = P_H - P(n), \quad (13)$$

where the subscript H refers to matching with the pQCD results. Then $P(n)$ should be within the ranges P_{min} and P_{max} already discussed.

In our interpolation, for the process of matching with pQCD it is important to take into account the value of the so-called critical chemical potential, μ_c , that corresponds to the pressure at the intersection point in the (n, μ) plane between the causal lines and the lower boundary of the branch connecting with pQCD at μ_H . Its expression is given by [40]:

$$\mu_c = \sqrt{\frac{\mu_L \mu_H (\mu_H n_H - \mu_L n_L - 2\Delta p)}{\mu_L n_H - \mu_H n_L}}. \quad (14)$$

where the subscript L denotes the low-density limit for this second extrapolation starting at n_s . If one considers velocities of sound $c_s^2 \leq 1$, this upper value cannot be held for chemical potentials $\mu \geq \mu_c$ in order to enter pQCD with $\mu_H = 2600$ MeV. Thus, we maintain the maximum velocity until we reach a potential $\mu_0 < \mu_c$ and, at this point, we link to pQCD by performing a long PT to the energy density value that allows reaching the pQCD band with a slope $c_s^2 \leq 1/3$. Other possibilities are also explored as, for example, instead of such a long PT we also allow a shorter one followed by an increase in $c_s^2 \leq 1$, and then repeating this process a few times, the number depending on the EoS within the limits settled by the allowed regions constructed from the first principles. After the final PT the pQCD limit is approached in the way just explained. In this work, we typically have that $\mu_0 \approx 2200$ MeV $< \mu_c = 2250$ MeV. For a lower slope case, such as $c_s^2 \leq 0.781$, $\mu_0 \approx 2020$ MeV, around a 10% lower than when allowing $c_s^2 \leq 1$. In both cases, $n(\mu_0)$ is less than or equal to the central density point in the star, when the TOV equations are solved.

Apart from these theoretical constraints coming from pQCD at very high densities, the intermediate density region (up to several times n_s , more details are given below) is further constrained with data from measurements on the mass-radius and tidal deformability of NSs.

Regarding masses, the heaviest neutron stars derive mainly from precise Shapiro time delay measurements of pulsars orbiting in binary systems, such as PSR J1614–2230 [7, 9], PSR J0348+0432 [8] and PSR J0740+6620 [9, 77], with reported masses $M \gtrsim 2M_\odot$. Furthermore, the heaviest neutron star observed is the black-widow pulsar PSR J0952-0607, which was recently reported by [78] with a mass at 68% confidence level.

PSR J0952-0607

$$M = 2.35 \pm 0.17 M_\odot \quad (15)$$

There are others sources of massive NS, such as the hypothesis that the remnant in GW170817, with a total mass $M = 2.82_{-0.09}^{+0.47} M_\odot$, collapsed to a black hole by data from the short gamma-ray burst GRB170817A [79]. Another example of massive NS is GW190425 [17], a GW signal candidate for black hole-neutron star merger, with a probable mass of the neutron star $M = 2.31_{-0.26}^{+0.56} M_\odot$.

On the other hand, the observation of a small NS in the supernova remnant HESS J1731-347 has been reported [80], with mass and radius at the 68% confidence level:

$$M = 0.77_{-0.17}^{+0.20} M_\odot, \quad R = 10.4_{-0.78}^{+0.86} \text{ km} \quad (16)$$

Additionally, masses and radii of NSs can be obtained from X-ray profiles of rotating hot-spot patterns measured with the NICER telescope. In this way, there are results for three NSs at 68%:

- PSR J0030+0451:

² $X = 3\bar{\Lambda}/\mu$, with $\bar{\Lambda}$ the $\overline{\text{MS}}$ renormalization scale

$$M = (1.34_{-0.16}^{+0.50}) M_{\odot}, R = (12.71_{-1.19}^{+1.14}) \text{ km} \quad [10] \quad (17)$$

$$M = (1.4 \pm 0.05) M_{\odot}, R = (13.02_{-1.06}^{+1.24}) \text{ km} \quad [11].$$

- PSR J0740+6620:

$$M = (2.08 \pm 0.07) M_{\odot}, R = (12.92_{-1.13}^{+2.09}) \text{ km} \quad [81] \quad (18)$$

$$M = (2.073 \pm 0.069) M_{\odot}, R = (12.49_{-0.88}^{+1.28}) \text{ km} \quad [82].$$

- PSR J0437-4715:

$$M = (1.418 \pm 0.037) M_{\odot}, R = (11.36_{-0.63}^{+0.95}) \text{ km} \quad [83]. \quad (19)$$

Another astrophysical input is the tidal deformability of NS in binary mergers [16, 84, 85]. An upper bound on the dimensionless binary tidal deformability parameter $\bar{\Lambda} \leq 720$ (low-spin priors) has been obtained from GW170817 [85]. A $1.4 M_{\odot}$ NS tidal deformability was deduced in [16] with the result:

$$\Lambda_{1.4} = 190_{-120}^{+390} \quad (20)$$

Further investigation on the GW170817 event together with electromagnetic signals [86] reported the following data for the individual NSs in the binary:

$$\begin{aligned} M &= 1.46_{-0.09}^{+0.13} M_{\odot}, \Lambda = 255_{-171}^{+416}, \\ M &= 1.26_{-0.12}^{+0.09} M_{\odot}, \Lambda = 661_{-375}^{+858}. \end{aligned} \quad (21)$$

The EoS is also constrained by forbidding a PT below $2.5n_s$. This constraint comes from the in-medium corrections of the quark condensate performed in [52, 87]. This quantity plays the role of an order parameter in nuclear matter, and depends on the value of the pion-nucleon sigma term ($\sigma_{\pi N}$). Higher values of $\sigma_{\pi N}$ favor the vanishing of the in-medium quark condensate at lower densities (as a first approximation the in-medium quark condensate depends linearly in $\sigma_{\pi N}$). For the largest phenomenological values $\sigma_{\pi N} \approx 60$ MeV [88, 89], one could have a vanishing of the in-medium quark condensate at $\approx 2.5n_s$. We just mention by passing that there is an ongoing tension sustained in time [90] between these phenomenological determinations and the ones from lattice QCD, which generate smaller values of $\sigma_{\pi N}$ somewhat above 40 MeV, like the recent calculation $\sigma_{\pi N} = 43.7 \pm 3.6$ MeV [91].

III. RESULTS

A. Interpolation up to the saturation density

The EoS from Ref. [36] is plotted in the left corner of Fig. 2 by the light green band up to its limit $n_L = 0.1n_s$.

Then, we proceed along the lines of the extrapolation method detailed in Sec. IIB for the low and intermediate density region up to $n = n_s$.

The EoS corresponding to the upper and lower limit points of the integral constraints corresponding to the first interpolation, taking as the highest value for the pressure at n_s either $P_s = 1.01$ MeV/fm³ ($L_{\text{sym}} = 19$ MeV) or 7.62 MeV/fm³ ($L_{\text{sym}} = 143$ MeV), are shown in Figure 2 by the palish yellow and blue areas, respectively. Growing the EoS through the grid points of the first interpolation, we find that the minimum EoS (red dashed line) compatible with $(E/A)_{UG}$ presents $P_s = 1.4$ MeV/fm³ at n_s , giving $L = 26.4$ MeV and $E/A = 13.3$ MeV. This value, in accordance with UGC, is smaller than the interval $(E/A)_{\text{PNM}}(n_s) \in (16.9, 27.3)$ MeV given in Eq. (12) from the phenomenological values of S_0 , L , $(E/A)_{\text{SNM}}(n_s)$ and n_s there discussed.

Finally, we take $P(n_s)$ from the red dashed line in Fig. 2 as the lower limit at n_s , and do the interpolation matching at n_s within the extreme values $P_{\text{high}} = 7.62$ MeV/fm³ and $P_{\text{low}} = 1.41$ MeV/fm³. The chemical potentials μ_H corresponding to these points are $\mu_H = 1014.5$ and 961.7 MeV, respectively. The allowed regions of EoS's stemming from the blue and red diamonds, corresponding to the former and latter pressures, respectively, are shown in Fig. 3 by the palish blue and yellow areas, in this order. For the interpolation process, we construct a 100-point EoS using a 1000×1000 -point grid to achieve better control over the slope. We construct the EoS's from the low-density band to the higher-density one by raising smoothly c_s^2 , keeping $dc_s^2/d\varepsilon > 0$, with this derivative being slightly larger or smaller depending on the point in the grid, until n_s is reached, where the interval of pressures between the extreme ones is filled. This gently rise in c_s^2 also avoids having to introduce PTs at too low densities because of touching the borders of the allowed region. We display the final band results for $P(\varepsilon)$ up to about n_s in Fig. 3. The value of L for the EoS that runs along the upper and lower limits of the total band corresponding to the red area in the figure are also given in the keys of the figure.

Our band of EoS's at this stage is also shown by the pink area in Fig. 4, compared with other calculations from quantum Monte Carlo [92] (blue dotted-dashed line), and the many-body perturbative methods with chiral potentials of Refs. [93, 94] (gray areas). In addition we also show by the red dashed line the unitary gas limit result.

B. Interpolation up to the pQCD regime

1. Without astrophysical observables

We discuss here the practical realization of the method explained in Secs. IIB and IID. We first apply the construction of Ref. [40] and determine the areas in the (ε, P)

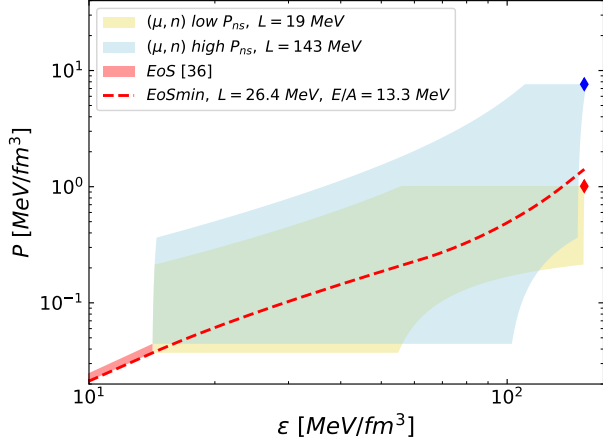


FIG. 2. Bounding areas of validity for PNM EoS by extrapolating the EoS of Ref. [36] (reddish band) from n_L up to n_s . The blue and red diamonds correspond to the highest chemical potentials used in the construction of Ref. [40], as explained in Sec. II B, for $L = 143$ MeV and 19 MeV, respectively. They give rise to the palish blue and yellow areas, in this order. The value $L \approx 25$ MeV is fixed by the UGC (as given above), closely approximated by the red dashed line.

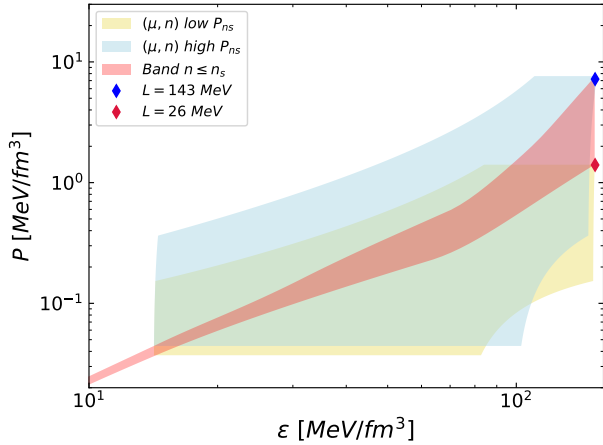


FIG. 3. Extrapolation from the upper limit of validity of the EoS [36] up to n_s , $n_L < n < n_s$. The same bounding bands of acceptable areas as in Fig. 2 are shown but now the read diamond is fixed from the red dashed line in Fig. 2. The resulting band of EoS's from the extrapolation up to n_s is the narrower red area.

plane inside which a viable EoS can interpolate between n_s and the pQCD region at around $40n_s$. At the lowest density we have the band determined in Sec. III A at n_s , within the two extreme pressure values 1.4 and 7.6 MeV/fm³, and shown in Fig. 3. At the highest density there is the band from the N³LO pQCD EoS [45, 48] at $n \approx 40n_s$, within the extreme pressures 2334 and 4384 MeV/fm³. In the process these areas for viable

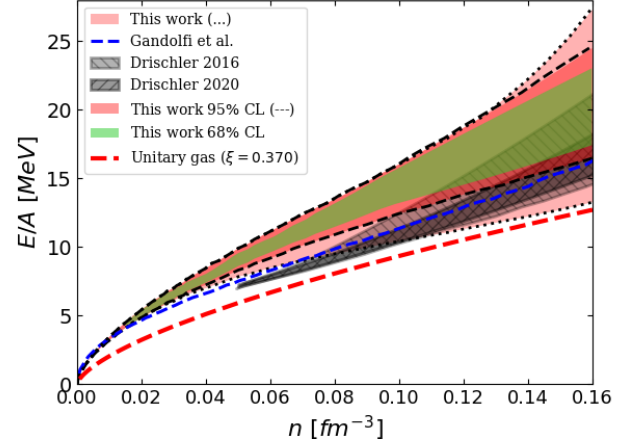


FIG. 4. We show our final band of EoS's up to n_s in three cases: The pink area corresponds to the direct extrapolation up to n_s , with its borders separated by dots. Once astrophysical constraints are taken into account the allowed area shrinks and it is depicted in green (68% CL) and in orange (95% CL), with the borders for the latter signaled by dashed lines. We also compare with other results: The blue dotted-dashed line is the Monte Carlo calculation of Ref. [92]. The many-body perturbation calculations from chiral potentials are given by the light [93] and darker [94] gray areas. The dashed one is the unitary limit for a Fermi gas.

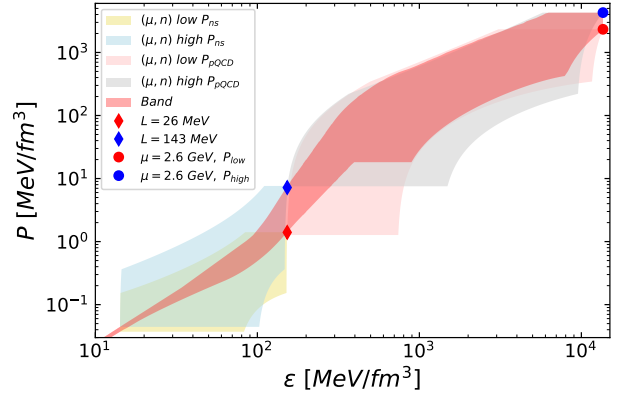


FIG. 5. Band obtained by interpolation from low to high densities, from the EoS [36] up to pQCD. This extrapolating band is limited only by first principles (causality and thermodynamical consistency), pQCD and from measurements of nuclear parameters.

EoS's connect the lowest and highest pressures at the extreme densities taken for the interpolation. These areas, and those already determined in Sec. III A for the extrapolation between n_L and n_s , are shown in Fig. 5. A $10^3 \times 10^3$ grid inside the region fulfilling Eq. (7) is built that in turn comprises these areas between n_s and $40n_s$ is built. We then construct each point of the EoS

$(n, E/A, \varepsilon, P, \mu)$ by applying the minimum slope growth, so that it maintains positive its derivative $dc_s^2/d\varepsilon > 0$, with slightly larger or smaller values depending on the point and the EoS, between $n_s \lesssim n \lesssim 2.5n_s$. In the interval $2n_s \leq n \leq 2.5n_s$ this derivative steadily increases for the stiffest EoS's that drive to preferred NS mass-radius relation according to present data, as we analyze in more detail below.

From $n > 2.5n_s$, in order to consider the possibility of PTs, we apply the condition $dc_s^2/d\varepsilon \geq 0$, allowing that it can be equal to zero. This derivative is smoothly increased until c_s^2 reaches its limit value, which is then kept until a chemical potential $\mu_0 < \mu_c = 2250$ MeV, for the causal value $c_s^2 \leq 1$, and $\mu_0 \lesssim 2040$ MeV $< \mu_c$ for the upper bound $c_s^2 \leq 0.781$ [64, 65]. For the case with PTs for $\mu < \mu_0$ we apply the limit value for c_s^2 between PTs in order to have a sufficiently stiff EoS. As discussed in Sec. IID, at the energy density corresponding to this high chemical potential, varying for each EoS, we consider different possibilities. One of them consists of making a long PT with an energy-density jump such that, from this PT onwards, pQCD is reached with $c_s^2 \rightarrow 1/3$ starting with $c_s^2 \approx 0.3$. Other interpolations involve a shorter PT followed by an increase in $c_s^2 \leq 1$, and then repeating this process again for a few times, depending of each EoS. After the final PT the pQCD limit is reached as explained before.

The resulting EoS band for a NS that follows from this interpolation procedure is depicted by the red area in Fig. 5 from the EoS [36] to the core and extended beyond up to pQCD, constrained only by causality, thermodynamical stability, pQCD and measurements from nuclear parameters. It is worth stressing that this band is not constrained by astrophysical observables and, as a result, it is convenient for testing GR and modify theories [95, 96]. We notice that for the soft EoS's, $n = 2.5n_s$ is reached for low values of P ($P < 50$ MeV/fm³), such that the EoS needs a specially fast increase of c_s^2 after the first PT. They also make other PTs for entering pQCD with $c_s^2 \leq 1/3$.

2. With astrophysical observables

Next, we take into account astrophysical observables in order to constrain further the EoS and apply GR to calculate them. We use the values of Mass and Radius of pulsars: PSR J0952-0607, Eq. (15), HESS J1731-347, Eq. (16), PSR J0030+0451, Eq. (17), PSR J0740+6620, Eq. (18), and PSR J0437-4715, Eq. (19). Solving together the Tolman-Oppenheimer-Volkoff (TOV) equations for non rotating-NS and tidal deformability equations for a variety of central pressures, the mass-radius relation, and the tidal-deformability/mass-radius relations are obtained for each given EoS.

We apply the method of least squares by using these six independent mass measurements M_i at known radius R_i (except for J0952-0607, see below) to obtain the band

of EoS's that minimizes the following χ^2 :

$$\chi^2 = \sum_{i=1}^6 \frac{(M_i - m(R_i))^2}{\sigma_i^2} \quad (22)$$

where the i_{th} mass measurement M_i is assumed to be Gaussian distributed with known variance σ_i^2 , while the theoretical calculation is represented by $m(R_i)$. All the σ_i values used correspond to the 68% confidence interval values derived from each analysis. If for an event they are asymmetrical, we take its left/right value if the point y_i is found to lie to the right/left of the theoretical band of values (a building up consistency criterion). For the case of PSR J0952-0607 its radius is not provided, cf. Eq. (15). Because of this, and regarding this pulsar, we can only demand that the EoS under consideration can generate NS masses large enough to accommodate its mass. Then, if the EoS considered generates a mass smaller than the upper bound for the mass of the PSR J0952-0607 ($M \geq 2.53 M_\odot$) we apply the standard definition for the contribution of this event to the χ^2 . If the highest allowed mass from this EoS is larger than the upper bound for the mass of the PSR J0952-0607 we do not add any contribution to the χ^2 from this mass measurement. Then, there is window for more massive NS, such as in the event GW190425.

For each EoS, we calculate in the way explained the χ^2 for the six measurements and select those EoS's whose χ^2 distribution reports a p -value ≥ 0.32 for 68% confidence level, and a p -value ≥ 0.05 for 95% confidence level. The set of EoS's with the former p -value makes the 68% band, while the set with the last p -value makes the 95% band.

The EoS bands obtained in the case of maximum value $c_s^2 \leq 1$ are shown at the top panel of Fig. 6 at the 68% CL (red band) and 95% CL (pink band). The resulting bands are much narrower than those in Fig. 5 before taking into account the astrophysical observables. It is worth stressing that, in this way, we can also constrain the nuclear observables, providing sharper values for the energy symmetry and its slope,

$$32.9 \leq S_0 \leq 39.5 \text{ MeV} ; 37.3 \leq L \leq 69.0 \text{ MeV (68\% CL)} , \quad (23)$$

$$32.1 \leq S_0 \leq 40.6 \text{ MeV} ; 34.6 \leq L \leq 80.0 \text{ MeV (95\% CL)} .$$

The interval for the obtained symmetry energy S_0 at 68 % remarkably lies inside 1σ PREX-II value, Eq. (9), and its slope L is almost at the one σ level for both scenarios of CREX, Eq. (11). Our range for S_0 at the 68% CL is compatible with $30 - 35$ MeV [97], $33_{-1.8}^{+2.0}$ [98], and 32 ± 1.7 MeV [71].

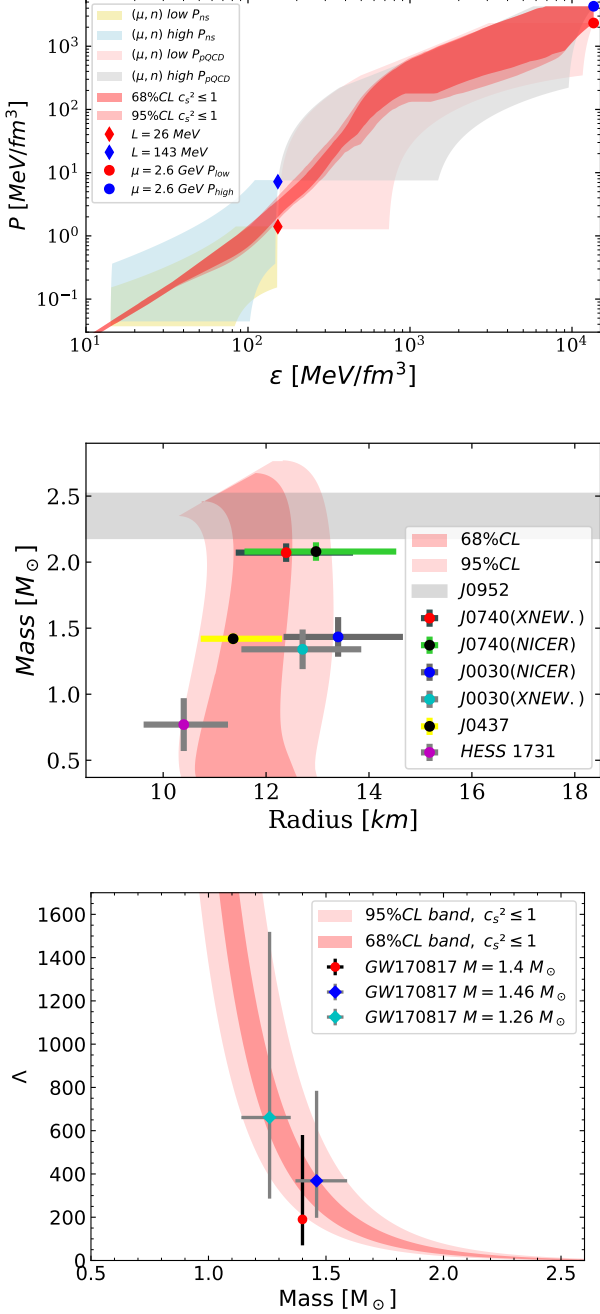


FIG. 6. **Top:** (ϵ, p) bands constrained from astrophysical observables at 68% CL (red) and 95% CL (pink) for $0 \leq c_s^2 \leq 1$. **Middle:** Mass-Radius diagrams for the EoS bands at the top. **Bottom:** Tidal deformability-Mass relation for the EoS bands at the top.

The calculated bands for the NS mass M in units of M_\odot as a function of its radius R in km at the 98% CL (red area) and 95% CL (pink area) are shown in the middle panel of Fig. 6. The different experimental values considered and discussed in Sec. IID are also indicated and explained in the keys of the figure. We see that the band within the one σ region is narrow, rather vertical, and

centered for a radius value somewhat below 12 km.

In the bottom panel of Fig. 6 we show within the same pattern the obtained tidal deformability Λ as a function of the NS mass in units of M_\odot confronted the experimental determinations from the GW170817 event [79] for three masses, 1.26, 1.4 and 1.36 M_\odot . We see that our resulting band of values agrees very well with the central values determined for 1.26 and 1.46 M_\odot , and it is compatible within one σ with the determination for 1.4 M_\odot .

Regarding maximal central values for quantities of interest in a NS, the chemical potential reaches values of $1420 \leq \mu_{c,\max} \leq 2220$ MeV at 68% CL, and within $1400 \leq \mu_{c,\max} \leq 2240$ MeV at 95% CL. With respect to the central baryon number density n_c , it varies in the interval $5.0n_s \leq n_c \leq 7n_s$ at 68% CL, and within $4.5n_s \leq n_c \leq 7.4n_s$ at 95% CL. For the energy per particle we find $280 \lesssim (E/A)_{c,\max} \lesssim 400$ MeV and $280 \lesssim (E/A)_{c,\max} \lesssim 430$ MeV at the 68% and 95% CL, respectively. All PTs that we find occur for $M \gtrsim 2.1 M_\odot$ both at 68 and 95 % CL, within the range of starting densities between $2.5n_s \leq n \leq n_c$. Both PTs with short and long phase-coexistence regions are found. For $c_s^2 \leq 1$, short PTs appear for $2.5n_s < n < 3.2n_s$ with $0.12 < \Delta n/n < 0.50$ (68% CL), and for $2.5n_s < n < 3.2n_s$ with $0.12 < \Delta n/n < 0.60$ (95% CL), and they typically require afterwards a steep rise in c_s^2 to confront well with NS mass-radius data. Because of this they could also stand for a second PT that starts at densities less than or equal to the central density of the NS. The longest PTs found have a phase-coexistence region that extends over a range of densities $3.4n_s \leq \Delta n \leq 19n_s$ at 68% CL, and $3.2n_s \leq \Delta n \leq 21n_s$ at 95% CL, such that $1 \lesssim \Delta n/n \leq 3.8$ at 68% CL and $1 \lesssim \Delta n/n \leq 4.5$ at 95% CL. Let us notice that Refs. [32, 33] conclude against the possible existence of PTs inside a NS with $M < 2.1 M_\odot$, in agreement with our results at 68% CL.

The top panel in Fig. 7 shows 4 EoS's at 68% CL with the same first PT at $P = 167$ MeV/fm³ and showing different ways to reach pQCD. For convenience, let us denote by $\tilde{\mu}$ the values of the chemical potential along the upper border line of the of the 68% CL region in the figure. Then, we consider EoS's with 2 PTs in total, such that a second PT at about $\tilde{\mu}$ takes place for the EoS represented by the dashed black line, while for the dotted gold line the second PT occurs below $\tilde{\mu}$. For 3 PTs in total we have the green line, with the second(third) PT happening below(about) $\tilde{\mu}$, while for the gold dashed line the 2 extra PTs happen both below $\tilde{\mu}$. Finally, we also plot by the red line an EoS with 4 PTs in total, with all the extra PTs below $\tilde{\mu}$. All these EoS's enter pQCD with $c_s^2 \leq 1/3$. For the bottom panel of Fig. 7 we depict 4 EoS's with several PTs all of them starting at densities inside the NS. The red and the two blue lines have 2 PTs, while the green line has 3 PTs. In between the blue dashed and dot-dashed lines other EoS's with this second PT of different length for the coexistence region could be considered as well.

The band of allowed EoS's for limiting $c_s^2 \leq 0.781$ [65, 65] is shown in the top panel of Fig. 8 up to typical central values of ε in a NS. We observe that until $\varepsilon \approx 450$ MeV/fm³ the resulting band is the same as the determined one in Fig. 6, but above this value the band starts becoming narrower. Now, for maximal central values we have a chemical potential $1390 \leq \mu_{c,\max} \leq 2020$ MeV at 68% CL and $1400 \leq \mu_{c,\max} \leq 2030$ MeV at 95% CL, a baryon number density $5.2n_s \leq n_c \leq 7.2n_s$ at 68% CL and $4.75n_s \leq n_c \leq 7.4n_s$ at 95% CL, with $(E/A)_{c,\max} \approx 280 - 385$ MeV in both cases. In this band of EoS we can find PTs with starting densities between $2.51n_s \leq n \leq n_c$. Within the interval of densities $2.51n_s < n < 3.3n_s$ at 68% CL, and between $2.51n_s < n < 3.3n_s$ at 95% CL, the PTS found show a co-existence range of baryon densities $0.15 \leq \Delta n \leq 0.65n_s$ of the short PT type. In the case of long PTs, occurring within the density interval $3.3n_s \leq n \leq 13.5n_s$ and $3.2n_s \leq n \leq 14n_s$ at 68% and 95%, respectively, the co-existence region extended over $1 \lesssim \Delta n/n \leq 2.6$ at 68% CL, and $1 \lesssim \Delta n/n \leq 3$ at 95% CL. Thus, since all these PTs report $1 \leq \Delta n/n$ they can be considered as strong first-order PTs [33]. The maximum-mass difference obtained between EoS's with limiting sound speed squared $c_s^2 \leq 1$ and $c_s^2 \leq 0.781$ is about 5–6%, being smaller for the latter. Since the maximum limit for c_s^2 applies for large enough density energy values above around 420 and 520 MeV/fm³ (which correspond to a star mass about $1.4 M_\odot$), the differences in the resulting values for the star radius can only be seen in the scale of the middle panel in Fig. 6 for $M > 2.1 M_\odot$. For instance, at the 68% CL, for $M = 2.18 M_\odot$ the maximum relative difference in the radius found is $\lesssim 1\%$, and for $M = 2.35 M_\odot$ one has a maximal relative difference of around 5.6%.

In the bottom panel of Fig. 8 we show the possible values of c_s^2 as a function of ε . The colored red and pink bands refer to the straight causal limit $c_s^2 \leq 1$ distinguishing between the 1σ and 2σ regions, respectively. Similarly, the dashed and dotted lines enclose the 1 and 2σ regions for the limit $c_s^2 \leq 0.781$, in this order. The dot-dashed lines show the results for two EoS's with the minimum χ^2 found for $c_s^2 \leq 1$. We observe that for $\varepsilon \lesssim 500$ MeV/fm³ the sound velocity squared increases within a relatively narrow band, but once PTs are considered for $n > 2.5n_s$ all feasible values for c_s^2 are registered by the resulting EoS. After the long PT for chemical potentials somewhat below $\mu_0 < \mu_c$ the sound velocity squared is limited by the conformal value $c_s^2 \leq 1/3$ to gradually reach the pQCD region.

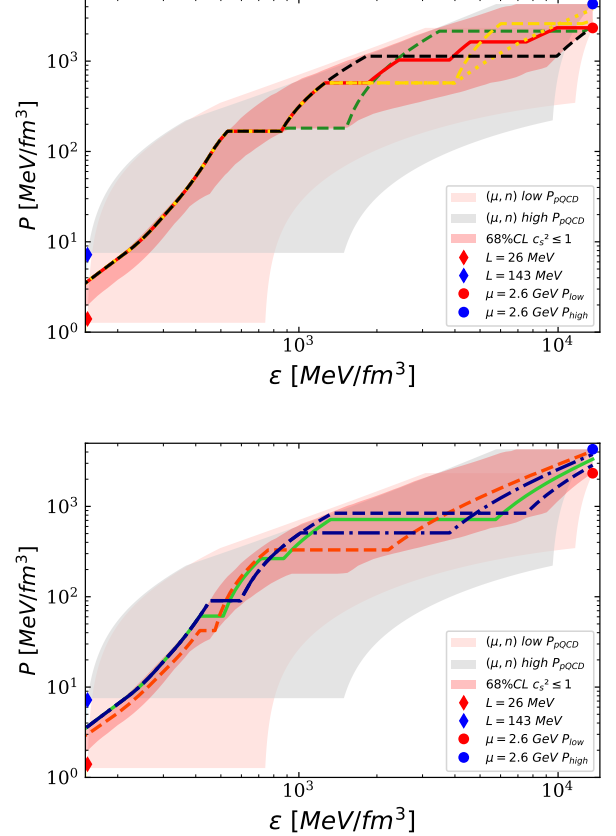


FIG. 7. All the EoS's considered in this plot are constrained from astrophysical observables at 68% CL for $0 \leq c_s^2 \leq 1$. **Top:** We plot 4 EoS's with the same first PT at $P = 167$ MeV/fm³ but reaching pQCD in distinct ways involving different number of PTs. **Bottom:** We show 3 EoS's with several PTs all of them starting at densities inside the NS. For the two panels see the text for the meaning of the lines and more details.

IV. SUMMARY AND CONCLUSIONS

In this work we have studied the equation of state (EoS) of a neutron star (NS) based on new results. On the theoretical side we use several recent developments of interest. In the low density range, for $n \leq 0.1n_s$, we have the recent calculation of the pure neutron matter EoS at low densities obtained by Ref. [36], being regulator independent and expressed directly in terms of experimental nucleon-nucleon scattering data. In the highest-density domain calculations in pQCD are now available up to $\mathcal{O}(\alpha_s^3)$ [43, 45, 48]. We then match between these two extremes by invoking first principles of causality and thermodynamic consistency and stability, following Refs. [40, 46]. On the experimental side, we take into account new measurements from PREX-II and CREX on the symmetry energy (S_0) and its slope (L) at saturation density, and observations and experimen-

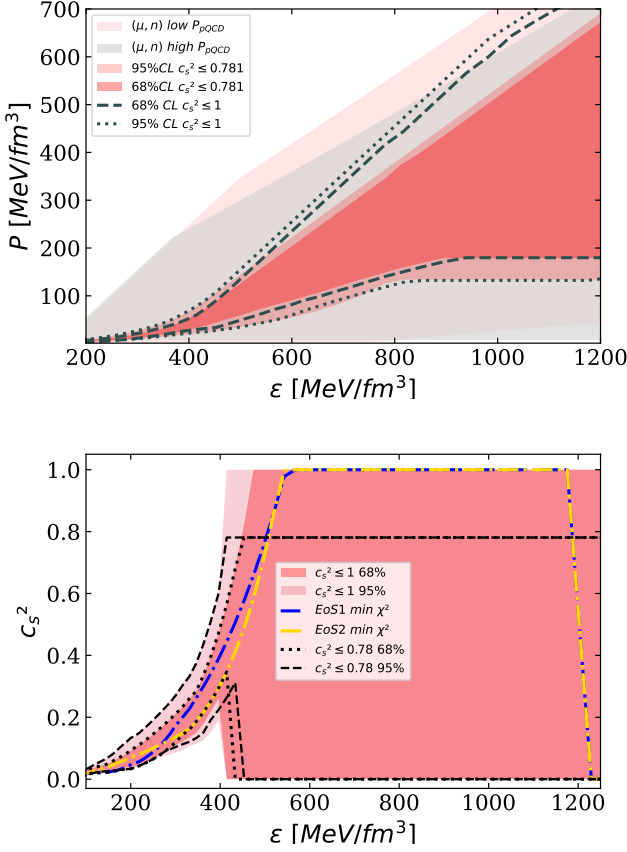


FIG. 8. All the EoS's considered in this plot are constrained by astrophysical observables. **Top:** Non-logarithmic bands of (ϵ, p) up to typical central densities inside a NS. The red band (dotted line) corresponds to our calculation with $c_s^2 \leq 0.781(1.0)$ at the 68% CL, and the pink one (dashed line) is similarly calculated at the 95% CL. **Bottom:** The distribution of c_s^2 as a function of ϵ . The red and pink bands correspond to the calculation at the 68% and 95% CL for $c_s^2 \leq 1$, respectively. In turn, the dashed and dotted lines correspond to $c_s^2 \leq 0.781$ with the same statistical meaning. We also show by the dot-dashed lines the results for two EoS's with the smallest χ^2 for $c_s^2 \leq 1$.

tal measurements of masses and radii of different neutron stars. By enforcing the EoS to satisfy all these theoretical and experimental requirements we obtain a band of EoS's that describes the data of NSs and tidal deformabilities. The band of EoS's obtained also constrains further the possible values of S_0 and L , narrowing the range of values of the latter by more than 50%. Our resulting values are $32.9 \leq S_0 \leq 39.5$ MeV and $37.3 \leq L \leq 69.0$ MeV at the 68% CL. The band of EoS's constructed in this way also indicates possible PTs for NS masses above $2.1 M_\odot$ at 68% CL, involving starting number densities above $2.5n_s$. We find both long and short coexistence regions during the PTs, corresponding to first and second order ones, respectively. Needless to say that the band of EoS's for NSs so determined can be used for research related to study other NS properties and dark matter capture in NSs.

We also calculate the band of EoS's when excluding the astrophysical observables in its determination, constrained only by causality, stability, pQCD and nuclear physics. Interestingly, our results can then be used to test GR and modified theories of gravity.

Our determined EoS's will be available at the ComPOSE database (<https://compose.obspm.fr/manual/>) [99–101].

ACKNOWLEDGEMENTS

We would like to thank Ingo Tews for providing us the data to plot the green band in Fig. 1. We also acknowledge partial financial support to the Grant PID2022-136510NB-C32 funded by MCIN/AEI/10.13039/501100011033/ and FEDER, UE, and to the EU Horizon 2020 research and innovation program, STRONG-2020 project, under grant agreement no. 824093.

-
- [1] A. Lovato *et al.*, (2022), [arXiv:2211.02224 \[nucl-th\]](#).
 - [2] N. F. Bell, G. Busoni, S. Robles, and M. Virgato, *JCAP* **09**, 028 (2020), [arXiv:2004.14888 \[hep-ph\]](#).
 - [3] C. A. Raithel, *Eur. Phys. J. A* **55**, 80 (2019), [arXiv:1904.10002 \[astro-ph.HE\]](#).
 - [4] G. Baym, H. A. Bethe, and C. Pethick, *Nucl. Phys. A* **175**, 225 (1971).
 - [5] J. W. Negele and D. Vautherin, *Nucl. Phys. A* **207**, 298 (1973).
 - [6] B. K. Sharma, M. Centelles, X. Viñas, M. Baldo, and G. F. Burgio, *Astron. Astrophys.* **584**, A103 (2015), [arXiv:1506.00375 \[nucl-th\]](#).
 - [7] P. B. Demorest, T. Pennucci, S. M. Ransom, M. S. E. Roberts, and J. H. T. Hessels, *Nature* **467**, 1081 (2010), [arXiv:1010.5788 \[astro-ph.HE\]](#).
 - [8] J. Antoniadis *et al.*, *Science* **340**, 1233232 (2013), [arXiv:1304.6875 \[astro-ph.HE\]](#).
 - [9] E. Fonseca *et al.*, *Astrophys. J. Lett.* **915**, L12 (2021), [arXiv:2104.00880 \[astro-ph.HE\]](#).
 - [10] T. E. Riley *et al.*, *Astrophys. J. Lett.* **887**, L21 (2019), [arXiv:1912.05702 \[astro-ph.HE\]](#).
 - [11] M. C. Miller *et al.*, *Astrophys. J. Lett.* **887**, L24 (2019), [arXiv:1912.05705 \[astro-ph.HE\]](#).
 - [12] T. E. Riley *et al.*, *Astrophys. J. Lett.* **918**, L27 (2021), [arXiv:2105.06980 \[astro-ph.HE\]](#).
 - [13] M. C. Miller *et al.*, *Astrophys. J. Lett.* **918**, L28 (2021), [arXiv:2105.06979 \[astro-ph.HE\]](#).

- [14] T. Salmi *et al.*, *Astrophys. J.* **941**, 150 (2022), [arXiv:2209.12840 \[astro-ph.HE\]](#).
- [15] B. P. Abbott *et al.*, *Phys. Rev. X* **9**, 011001 (2019), [arXiv:1805.11579 \[gr-qc\]](#).
- [16] B. P. Abbott *et al.*, *Phys. Rev. Lett.* **121**, 161101 (2018), [arXiv:1805.11581 \[gr-qc\]](#).
- [17] B. P. Abbott *et al.* (LIGO Scientific, Virgo), *Astrophys. J. Lett.* **892**, L3 (2020), [arXiv:2001.01761 \[astro-ph.HE\]](#).
- [18] H. Koehn *et al.*, (2024), [arXiv:2402.04172 \[astro-ph.HE\]](#).
- [19] E. Annala, T. Gorda, A. Kurkela, J. Nättilä, and A. Vuorinen, *Nat. Phys.* **16**, 907 (2020), [arXiv:1903.09121 \[astro-ph.HE\]](#).
- [20] G. Raaijmakers, S. K. Greif, K. Hebeler, T. Hinderer, S. Nissanke, A. Schwenk, T. E. Riley, A. L. Watts, J. M. Lattimer, and W. C. G. Ho, *Astrophys. J. Lett.* **918**, L29 (2021), [arXiv:2105.06981 \[astro-ph.HE\]](#).
- [21] P. T. H. Pang, I. Tews, M. W. Coughlin, M. Bulla, C. van den Broeck, and T. Dietrich, (2021), [arXiv:2105.08688 \[astro-ph.HE\]](#).
- [22] I. Legred, K. Chatziioannou, R. Essick, S. Han, and P. Landry, *Phys. Rev. D* **104**, 063003 (2021), [arXiv:2106.05313 \[astro-ph.HE\]](#).
- [23] B. Biswas, *Astrophys. J.* **921**, 63 (2021), [arXiv:2105.02886 \[astro-ph.HE\]](#).
- [24] B. Biswas and S. Datta, *Phys. Rev. D* **106**, 043012 (2022), [arXiv:2112.10824 \[astro-ph.HE\]](#).
- [25] C. Ecker and L. Rezzolla, *Mon. Not. Roy. Astron. Soc.* **519**, 2615 (2022), [arXiv:2209.08101 \[astro-ph.HE\]](#).
- [26] S. Altiparmak, C. Ecker, and L. Rezzolla, *Astrophys. J. Lett.* **939**, L34 (2022), [arXiv:2203.14974 \[astro-ph.HE\]](#).
- [27] S. Huth *et al.*, *Nature* **606**, 276 (2022), [arXiv:2107.06229 \[nucl-th\]](#).
- [28] E. Annala, T. Gorda, J. Hirvonen, O. Komoltsev, A. Kurkela, J. Nättilä, and A. Vuorinen, *Nature Commun.* **14**, 8451 (2023), [arXiv:2303.11356 \[astro-ph.HE\]](#).
- [29] R. Somasundaram, I. Tews, and J. Margueron, *Phys. Rev. C* **107**, 025801 (2023), [arXiv:2112.08157 \[nucl-th\]](#).
- [30] R. Essick, I. Legred, K. Chatziioannou, S. Han, and P. Landry, *Phys. Rev. D* **108**, 043013 (2023), [arXiv:2305.07411 \[astro-ph.HE\]](#).
- [31] Y. Lim and J. W. Holt, *Galaxies* **10**, 99 (2022), [arXiv:2204.09000 \[nucl-th\]](#).
- [32] L. Brandes, W. Weise, and N. Kaiser, *Phys. Rev. D* **108**, 094014 (2023), [arXiv:2306.06218 \[nucl-th\]](#).
- [33] L. Brandes and W. Weise, *Symmetry* **16**, 111 (2024), [arXiv:2312.11937 \[nucl-th\]](#).
- [34] S.-P. Tang, M.-Z. Han, Y.-J. Huang, Y.-Z. Fan, and D.-M. Wei, *Phys. Rev. D* **109**, 083037 (2024), [arXiv:2311.13805 \[astro-ph.HE\]](#).
- [35] F. J. Llanes-Estrada and E. Lope-Oter, *Prog. Part. Nucl. Phys.* **109**, 103715 (2019), [arXiv:1907.12760 \[nucl-th\]](#).
- [36] J. M. Alarcón and J. A. Oller, *Phys. Rev. C* **107**, 044319 (2023), [arXiv:2212.05092 \[nucl-th\]](#).
- [37] D. J. Thouless, *Ann. Phys.* **10**, 553 (1960).
- [38] J. M. Alarcon and J. A. Oller, *Annals Phys.* **437**, 168741 (2022), [arXiv:2106.02652 \[nucl-th\]](#).
- [39] J. M. Alarcón and J. A. Oller, *Phys. Rev. C* **106**, 054003 (2022), [arXiv:2107.08051 \[cond-mat.quant-gas\]](#).
- [40] O. Komoltsev and A. Kurkela, *Phys. Rev. Lett.* **128**, 202701 (2022), [arXiv:2111.05350 \[nucl-th\]](#).
- [41] D. Adhikari *et al.* (PREX), *Phys. Rev. Lett.* **126**, 172502 (2021), [arXiv:2102.10767 \[nucl-ex\]](#).
- [42] D. Adhikari *et al.* (CREX), *Phys. Rev. Lett.* **129**, 042501 (2022), [arXiv:2205.11593 \[nucl-ex\]](#).
- [43] A. Kurkela, P. Romatschke, and A. Vuorinen, *Phys. Rev. D* **81**, 105021 (2010), [arXiv:0912.1856 \[hep-ph\]](#).
- [44] E. S. Fraga, A. Kurkela, and A. Vuorinen, *Astrophys. J. Lett.* **781**, L25 (2014), [arXiv:1311.5154 \[nucl-th\]](#).
- [45] T. Gorda, A. Kurkela, R. Paatelainen, S. Säppi, and A. Vuorinen, *Phys. Rev. D* **104**, 074015 (2021), [arXiv:2103.07427 \[hep-ph\]](#).
- [46] E. Lope Oter, A. Windisch, F. J. Llanes-Estrada, and M. Alford, *J. Phys. G* **46**, 084001 (2019), [arXiv:1901.05271 \[gr-qc\]](#).
- [47] E. Lope-Oter and F. J. Llanes-Estrada, *Eur. Phys. J. A* **58**, 9 (2022), [arXiv:2108.04027 \[hep-ph\]](#).
- [48] T. Gorda, A. Kurkela, R. Paatelainen, S. Säppi, and A. Vuorinen, *Phys. Rev. Lett.* **127**, 162003 (2021), [arXiv:2103.05658 \[hep-ph\]](#).
- [49] C. Drischler, J. A. Melendez, R. J. Furnstahl, and D. R. Phillips, *Phys. Rev. C* **102**, 054315 (2020), [arXiv:2004.07805 \[nucl-th\]](#).
- [50] C. Drischler, K. Hebeler, and A. Schwenk, *Phys. Rev. Lett.* **122**, 042501 (2019), [arXiv:1710.08220 \[nucl-th\]](#).
- [51] R. Navarro Pérez, J. E. Amaro, and E. Ruiz Arriola, *J. Phys. G* **43**, 114001 (2016), [arXiv:1410.8097 \[nucl-th\]](#).
- [52] U. G. Meißner, J. A. Oller, and A. Wirzba, *Annals Phys.* **297**, 27 (2002), [arXiv:nucl-th/0109026](#).
- [53] J. A. Oller, A. Lacour, and U. G. Meißner, *J. Phys. G* **37**, 015106 (2010), [arXiv:0902.1986 \[nucl-th\]](#).
- [54] J. A. Oller, *J. Phys. G* **46**, 073001 (2019), [arXiv:1902.06065 \[nucl-th\]](#).
- [55] A. Lacour, J. A. Oller, and U. G. Meißner, *Annals Phys.* **326**, 241 (2011), [arXiv:0906.2349 \[nucl-th\]](#).
- [56] K. Hebeler, S. K. Bogner, R. J. Furnstahl, A. Nogga, and A. Schwenk, *Phys. Rev. C* **83**, 031301 (2011), [arXiv:1012.3381 \[nucl-th\]](#).
- [57] S. Huth, C. Wellenhofer, and A. Schwenk, *Phys. Rev. C* **103**, 025803 (2021), [arXiv:2009.08885 \[nucl-th\]](#).
- [58] B. Friedman and V. R. Pandharipande, *Nucl. Phys. A* **361**, 502 (1981).
- [59] G. Wlazłowski, J. W. Holt, S. Moroz, A. Bulgac, and K. J. Roche, *Phys. Rev. Lett.* **113**, 182503 (2014), [arXiv:1403.3753 \[nucl-th\]](#).
- [60] A. Gezerlis and J. Carlson, *Phys. Rev. C* **77**, 032801 (2008), [arXiv:0711.3006 \[nucl-th\]](#).
- [61] A. Gezerlis, I. Tews, E. Epelbaum, S. Gandolfi, K. Hebeler, A. Nogga, and A. Schwenk, *Phys. Rev. Lett.* **111**, 032501 (2013), [arXiv:1303.6243 \[nucl-th\]](#).
- [62] E. Epelbaum, H. Krebs, D. Lee, and U.-G. Meißner, *Eur. Phys. J. A* **40**, 199 (2009), [arXiv:0812.3653 \[nucl-th\]](#).
- [63] I. Tews, T. Krüger, K. Hebeler, and A. Schwenk, *Phys. Rev. Lett.* **110**, 032504 (2013), [arXiv:1206.0025 \[nucl-th\]](#).
- [64] M. Hippert, J. Noronha, and P. Romatschke, (2024), [arXiv:2402.14085 \[nucl-th\]](#).
- [65] S.-P. Tang, Y.-J. Huang, M.-Z. Han, and Y.-Z. Fan, (2024), [arXiv:2404.09563 \[astro-ph.HE\]](#).
- [66] B. T. Reed, F. J. Fattoyev, C. J. Horowitz, and J. Piekarewicz, *Phys. Rev. Lett.* **126**, 172503 (2021), [arXiv:2101.03193 \[nucl-th\]](#).
- [67] B. T. Reed, F. J. Fattoyev, C. J. Horowitz, and J. Piekarewicz, *Phys. Rev. C* **109**, 035803 (2024), [arXiv:2305.19376 \[nucl-th\]](#).

- [68] M. Bender, P.-H. Heenen, and P.-G. Reinhard, *Rev. Mod. Phys.* **75**, 121 (2003).
- [69] Z. Zhang and L.-W. Chen, *Phys. Rev. C* **108**, 024317 (2023), [arXiv:2207.03328 \[nucl-th\]](#).
- [70] I. Tews, J. M. Lattimer, A. Ohnishi, and E. E. Kolomeitsev, *Astrophys. J.* **848**, 105 (2017), [arXiv:1611.07133 \[nucl-th\]](#).
- [71] J. M. Lattimer, *J. Phys. Conf. Ser.* **2536**, 012009 (2023), [arXiv:2308.08001 \[nucl-th\]](#).
- [72] G. Zuern, T. Lompe, A. Wenz, S. Jochim, P. Julienne, and J. Hutson, *Phys. Rev. Lett.* **110**, 135301 (2013).
- [73] A. Kurkela and A. Vuorinen, *Phys. Rev. Lett.* **117**, 042501 (2016), [arXiv:1603.00750 \[hep-ph\]](#).
- [74] T. Gorda, R. Paatelainen, S. Säppi, and K. Seppänen, *Phys. Rev. Lett.* **131**, 181902 (2023), [arXiv:2307.08734 \[hep-ph\]](#).
- [75] R. Somasundaram, I. Tews, and J. Margueron, *Phys. Rev. C* **107**, L052801 (2023), [arXiv:2204.14039 \[nucl-th\]](#).
- [76] T. Gorda, O. Komoltsev, and A. Kurkela, *Astrophys. J.* **950**, 107 (2023), [arXiv:2204.11877 \[nucl-th\]](#).
- [77] H. T. Cromartie *et al.*, *Nat. Astron.* **4**, 72 (2020), [arXiv:1904.06759 \[astro-ph.HE\]](#).
- [78] R. W. Romani, D. Kandel, A. V. Filippenko, T. G. Brink, and W. Zheng, *Astrophys. J. Lett.* **934**, L18 (2022), [arXiv:2207.05124 \[astro-ph.HE\]](#).
- [79] B. P. Abbott *et al.* (LIGO Scientific, Virgo, Fermi GBM, INTEGRAL, IceCube, AstroSat Cadmium Zinc Telluride Imager Team, IPN, Insight-Hxmt, ANTARES, Swift, AGILE Team, 1M2H Team, Dark Energy Camera GW-EM, DES, DLT40, GRAWITA, Fermi-LAT, ATCA, ASKAP, Las Cumbres Observatory Group, OzGrav, DWF (Deeper Wider Faster Program), AST3, CAASTRO, VINROUGE, MASTER, J-GEM, GROWTH, JAGWAR, CaltechNRAO, TTU-NRAO, NuSTAR, Pan-STARRS, MAXI Team, TZAC Consortium, KU, Nordic Optical Telescope, ePESSTO, GROND, Texas Tech University, SALT Group, TOROS, BOOTES, MWA, CALET, IKI-GW Follow-up, H.E.S.S., LOFAR, LWA, HAWC, Pierre Auger, ALMA, Euro VLBI Team, Pi of Sky, Chandra Team at McGill University, DFN, ATLAS Telescopes, High Time Resolution Universe Survey, RIMAS, RATIR, SKA South Africa/MeerKAT), *Astrophys. J. Lett.* **848**, L12 (2017), [arXiv:1710.05833 \[astro-ph.HE\]](#).
- [80] V. Doroshenko, V. Suleimanov, G. Pühlhofer, and A. Santangelo, *Nature Astronomy* **6**, 1444 (2022).
- [81] A. J. Dittmann *et al.*, (2024), [arXiv:2406.14467 \[astro-ph.HE\]](#).
- [82] T. Salmi *et al.*, (2024), [arXiv:2406.14466 \[astro-ph.HE\]](#).
- [83] D. Choudhury *et al.*, *Astrophys. J. Lett.* **971**, L20 (2024), [arXiv:2407.06789 \[astro-ph.HE\]](#).
- [84] B. P. Abbott *et al.*, *Phys. Rev. Lett.* **119**, 161101 (2017), [arXiv:1710.05832 \[gr-qc\]](#).
- [85] B. P. Abbott *et al.* (LIGO Scientific, Virgo), *Phys. Rev. X* **9**, 011001 (2019), [arXiv:1805.11579 \[gr-qc\]](#).
- [86] M. Fasano, T. Abdelsalhin, A. Maselli, and V. Ferrari, *Phys. Rev. Lett.* **123**, 141101 (2019), [arXiv:1902.05078 \[astro-ph.HE\]](#).
- [87] A. Lacour, J. A. Oller, and U. G. Meißner, *J. Phys. G* **37**, 125002 (2010), [arXiv:1007.2574 \[nucl-th\]](#).
- [88] J. M. Alarcon, J. Martin Camalich, and J. A. Oller, *Phys. Rev. D* **85**, 051503 (2012), [arXiv:1110.3797 \[hep-ph\]](#).
- [89] M. Hoferichter, J. Ruiz de Elvira, B. Kubis, and U.-G. Meißner, *Phys. Rev. Lett.* **115**, 092301 (2015), [arXiv:1506.04142 \[hep-ph\]](#).
- [90] J. M. Alarcón, *Eur. Phys. J. ST* **230**, 1609 (2021), [arXiv:2205.01108 \[hep-ph\]](#).
- [91] A. Agadjanov, D. Djukanovic, G. von Hippel, H. B. Meyer, K. Ottinad, and H. Wittig, *Phys. Rev. Lett.* **131**, 261902 (2023), [arXiv:2303.08741 \[hep-lat\]](#).
- [92] S. Gandolfi, J. Carlson, and S. Reddy, *Phys. Rev. C* **85**, 032801 (2012), [arXiv:1101.1921 \[nucl-th\]](#).
- [93] C. Drischler, A. Carbone, K. Hebeler, and A. Schwenk, *Phys. Rev. C* **94**, 054307 (2016), [arXiv:1608.05615 \[nucl-th\]](#).
- [94] C. Drischler, R. J. Furnstahl, J. A. Melendez, and D. R. Phillips, *Phys. Rev. Lett.* **125**, 202702 (2020), [arXiv:2004.07232 \[nucl-th\]](#).
- [95] E. Lope-Oter and A. Wojnar, *JCAP* **02**, 017 (2024), [arXiv:2306.00870 \[gr-qc\]](#).
- [96] E. Lope-Oter and A. Wojnar, (2024), [arXiv:2402.03914 \[gr-qc\]](#).
- [97] X. Roca-Maza, X. Viñas, M. Centelles, B. K. Agrawal, G. Colo', N. Paar, J. Piekarewicz, and D. Vretenar, *Phys. Rev. C* **92**, 064304 (2015), [arXiv:1510.01874 \[nucl-th\]](#).
- [98] R. Essick, I. Tews, P. Landry, and A. Schwenk, (2021), [arXiv:2102.10074 \[nucl-th\]](#).
- [99] S. Typel *et al.* (CompOSE Core Team), *Eur. Phys. J. A* **58**, 221 (2022), [arXiv:2203.03209 \[astro-ph.HE\]](#).
- [100] M. Oertel, M. Hempel, T. Klähn, and S. Typel, *Rev. Mod. Phys.* **89**, 015007 (2017), [arXiv:1610.03361 \[astro-ph.HE\]](#).
- [101] S. Typel, M. Oertel, and T. Klähn, *Phys. Part. Nucl.* **46**, 633 (2015), [arXiv:1307.5715 \[astro-ph.SR\]](#).